Journal of Materials Chemistry A

Accepted Manuscript

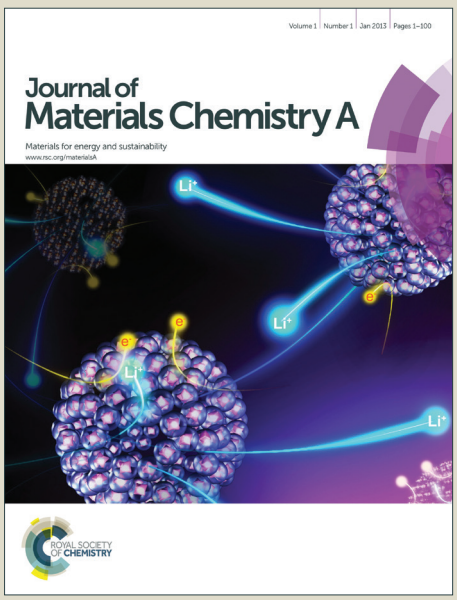

ROYAL SOCIETY OF CHEMISTRY

www.rsc.org/materialsA

Journal of Materials Chemistry A

Dynamic Article Links ►

Cite this: DOI: 10.1039/c0xx00000x

ARTICLE TYPE

www.rsc.org/xxxxxx

Carbon encapsulated 3D hierarchical Fe_3O_4 spheres as an advanced anode material with long cycle lifetimes for lithium-ion batteries

Xiulin Fan, Jie Shao, Xuezhang Xiao, Lixin Chen,* Xinhua Wang, Shouquan Li, Hongwei Ge

Received (in XXX, XXX) Xth XXXXXXXXX 20XX, Accepted Xth XXXXXXXXX 20XX

DOI: 10.1039/b000000x

As anode materials for lithium ion batteries, metal oxides have a large storage capacity. However, their cycle life and rate capability are still not suitable for commercial applications. Herein, 3D hierarchical Fe_3O_4 spheres associated with a 5-10 nm carbon shell were designed and fabricated. In the constructed architecture, the thin carbon shells can avoid the direct exposure of encapsulated Fe_3O_4 to the electrolyte and preserve the structural and electrochemical integrity of spheres as well as inhibit the aggregation of pulverized Fe_3O_4 during electrochemical cycling. While the hierarchical structure formed by bottom-up self-assembly approach can efficiently accommodate the mechanical stress induced by the severe volume variation of Fe_3O_4 during lithiation/delithiation processes. Moreover, the carbon shell together with the structure integrity and durability endows the favorable high conductivity and efficient ion transport. All of these features are critical for high-performance anodes, therefore enables an outstanding lithium storage performance with long cycle lifespan. For instance, such an electrode could deliver a capacity of 910 mAh g^{-1} even after 600 cycles with a discharge/charge rate of 1 A g^{-1}. In addition, this effective strategy may be readily extended to construct many other classes of hybrid electrode materials for high-performance lithium-ion batteries

1. Introduction

Due to the demand of renewable energy sources for extensive applications, from consumer electronics to electrical vehicles, materials for electrodes of lithium ion batteries (LIBs) have been intensively explored.[1] Currently, commercial anodes are made of graphite. However, its energy density is too low (372 mAh g^{-1}) and using graphite imposes safety issues because of the lower operating voltage.[2] In the last two decades, a worldwide effort has been made to search for alternative anode materials for higher energy density and longer cycle lifetimes. Recently, Sony introduced amorphous phase of a Sn-Co alloy with carbon as anode electrode, which showed a remarkable improvement for the anode materials with a capacity of ~600 mAh g^{-1}.[3] Among the explored systems, iron oxide has been considered as one of the most promising anode candidates because of its higher reversible specific capacity (~ 1000 mAh g^{-1}), world-wide abundance, high corrosion resistance, low cost and non-toxic properties.[4] However, significant capacity fading is observed at both high rate and long-term electrochemical cycling due to the excessive generation of solid-electrolyte interphase (SEI) layers on the surface, low electrical conductivity of its intrinsic nature, and mechanical degradation and pulverization resulted from severe volume expansion and contraction (~ 200%) during cycling.[5]

To address these intractable issues, two typical approaches have been employed. One effective method is to fabricate nanostructured iron oxide materials with various morphologies,[4a, 6] including nanoparticles,[7] nanospheres,[8] nanorods,[9] nanosheets,[10] nanotubes,[11] etc. Of particular note, the hierarchical structures have aroused tremendous interest because of their intrinsic merits[4a, 12]: 1) the hierarchical structure provides extra free void for alleviating the structural strain and accommodating the large volume variation during repeated electrochemical discharge and charge processes; 2) the relatively high surface area endows the materials with more lithium storage sites and large electrode-electrolyte contact area for high lithium ions flux across the interface. Although, improved the cycling performance was achieved compared with the solid counterpart.[11, 13] The rate capability still remains insufficient to fully realize its potential in LIBs due to intrinsically poor electronic conductivity of iron oxide.[14] Besides, excessive generation of SEI films on the surface of active structures will consume much of the lithium supplied by the cathodes and cause crack-up of the nanostructures.[15] The other promising strategy is to construct hybrid electrodes by integrating the carbonaceous matrix into the iron oxide active materials to form hybrid nanostructures.[1a, 2b, 4a, 6b, 16] By coating a thin carbon layer on the iron oxide nanostructures, which accounts for limited weight percent, significantly enhanced electrochemical performance can be achieved. The carbon can promote the electron transport in the poorly conductive iron oxide, form a stable SEI film and

meanwhile act as buffer layers to enhance the stability of the electrode materials.[17] However, the compact carbon coatings cannot allow residual buffer space to relieve the critical stress arising from the large volume change during Li^+ insertion/ extraction,[18] which will eventually induce the collapse of shells after prolonged cycles.[16b] It would be highly desirable to synthesize Fe_3O_4@carbon core shell architecture with hierarchical structure, which can fully utilize the merits of hierarchical structure and carbon coating mentioned above.

Herein, we develop a novel hierarchical Fe_3O_4@carbon core-shell structure as an advanced anode material for LIBs. The as-synthesized composite provides the critical features that are required for high-performance anodes, including efficient ion transport, high conductivity, favorable structure integrity and durability, therefore enabling an outstanding lithium storage performance with long cycle lifespan.

Experimental Section

2.1 Preparation of Fe_3O_4 hierarchical Spheres.

In a typical experiment, first, 0.64 g (1.84 mmol) of sodium dodecyl benzene sulfonate (SDBS) surfactant in ethylene glycol (64 mL) was stirred vigorously at room temperature to give a transparent solution. Next, 2.16 g (8 mmol) of $FeCl_3 \cdot 6H_2O$ and 3.72 g (44 mmol) of sodium acetate were added to the solution with vigorous stirring. Then the solution was transferred into a Teflon-lined stainless-steel autoclave with volume of 100 ml, and subsequently sealed and heated at 190 °C for 15 h in an oven. The resulting black product was centrifuged and washed with deionized water several times, and dried at 60 °C under vacuum overnight.

2.2 Preparation of Carbon coated Fe_3O_4 Spheres

A 0.8 g Fe_3O_4 nanoparticles was dispersed in 12.5 mL deionized water by ultrasonication to form a suspension. 1.6 g glucose was dissolved in another 37.5 mL deionized water. The former suspension together with 25 mL ethanol was added to the solution under stirring. The resulting suspension was transferred into a Teflon-lined stainless-steel autoclave with volume of 100 ml, and subsequently sealed and heated at 190 °C for 12 h in an oven. The carbon-precursor coated Fe_3O_4 hollow nanoparticles were washed with deionized water and dried at 90 °C in an oven. The resulting sample was heated in a quartz tube at 600 °C in Ar atmosphere for 4 h.

2.3 Characterization

X-ray diffraction (XRD) experiments of the samples were performed on an X'Pert Pro X-ray diffractometer (PANalytical, the Netherlands) with Cu K_α radiation at 40 kV and 40 mA. X-ray photoelectron spectroscopy (XPS) was carried out on a VG ESCALAB MARK II system with Mg K_α radiation (1253.6 eV) at a base pressure of 1×10^{-8} Torr. All binding energy values were referenced to the C 1s peak of carbon at 284.6 eV with an uncertainty of ±0.2 eV. Transmission electron microscopy (TEM, Tecnai G2 F30) and Scanning electron microscopy (SEM, Hitachi SU-70) were performed to examine the morphology and microstructure of the products. The accelerating voltage of TEM is 300 kV. For the cycled anode materials, before TEM characterization, the electrode was first washed with the electrolyte and then untrasonically dispersed in the ethanol to prepare the testing sample. Specific surface areas, pore size distributions, and pore volumes for the samples were characterized with N_2 adsorption by means of a Quantacrome Autosorb-1-C system using the Brunauer-Emmett-Teller (BET) and Barrett-Joyner-Halenda (BJH) methods. Thermogravimetric analysis (TGA, Netzsch STA 449F3), performed in air with a heating rate of 3 °C/min, was used to determine the chemical composition of hybrid Fe_3O_4@C composite.

The electrochemical tests were performed using a coin-type half cell (CR 2025). Metallic lithium was used as the negative electrode. To prepare working electrodes, Fe_3O_4@C or Fe_3O_4 powders, carbon black, styrene-butadiene rubber (SBR) and sodium carboxymethyl cellulose (CMC) with mass ratio 90:5:2.5:2.5 were mixed into a homogeneous slurry in deionized water with pestle and mortar. The slurry mixture was coated onto Cu foil and then dried at 80 °C for 12 h under vacuum. The electrolyte solution comprised 1 M $LiPF_6$/ethylene carbonate (EC)/ dimethyl carbonate (DMC)/ ethylmethyl carbonate (EMC) (1:1:1 by volume). The cells were assembled with a polypropylene (PP) microporous film (Celgard 2300) as the separator. Charge/discharge experiments were performed at a constant current density between 0.005 and 3 V using a LAND CT2001A Battery Cycler at room temperature. Cyclic voltammetry (CV) was performed on the CHI660E electrochemical workstation in the potential range 0-3.0 V (vs Li^+/Li) at a scan rate of 0.1 mV/s. For the electrochemical impedance spectroscopy (EIS) measurements, the excitation voltage applied to the cell was 5 mV and the frequency range was from 100 kHz to 10 mHz.

3. Results and discussion

The overall synthetic procedures of 3D hierarchical Fe_3O_4@C core-shell spheres are illustrated in Scheme 1. Fe_3O_4 nanoparticles stabilized with SDBS were first prepared by alcohol reduction of ferric chloride via a solvothermal process. Then, Fe_3O_4 nanoparticles will be assembled into a hierarchical sphere with size of ≈ 200 nm in the autoclave. After synthesis of spheres, a carbon shell with thickness of several nanometers was coated using glucose solution as carbon precursor, detailed procedures are presented in experimental section.

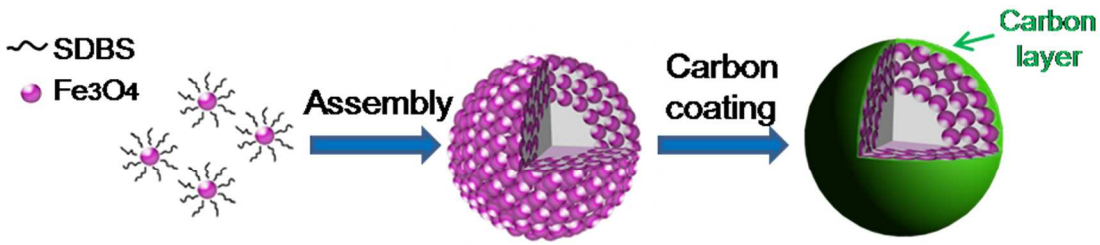

Scheme 1 Schematic representation of the preparation of hierarchical Fe_3O_4@C spheres.

SEM (Figure 1a, Figure S1) and TEM (Figure 1b) images show that Fe_3O_4 spheres with diameters of 200 nm were assembled by primary particles with size of ~20 nm. The high resolution TEM (HRTEM) is shown in Figure 1c, which confirmed the well crystallization of Fe_3O_4 nanoparticles, and no other layers on the surface of Fe_3O_4 nanoparticles. Lattice fringes with a spacing of 0.30 nm can be seen from the HRTEM image, corresponding to the (220) planes of Fe_3O_4. These results indicate that large-scale production of uniform-sized Fe_3O_4 spheres can be achieved in a simple way with the assistant of SDBS.

The hierarchical structure was well maintained after the carbon coating procedure. SEM (Figure 1d) and TEM (Figure 1e) images clearly demonstrate typical Fe_3O_4 spheres are tightly encapsulated by carbon layers. The core-shell feature can further be elucidated from representative HRTEM image that there is notable contrast between the Fe_3O_4 nanoparticles and carbon shells, as shown in Figure 1f. Crystalline Fe_3O_4 is well encapsulated by amorphous carbon layers (5-10 nm). Of particular note, comparing to Fe_3O_4 spheres, it shows that the size of primary constituent nanoparticles of Fe_3O_4 in Fe_3O_4@C hybrids become more uniform with the spherical morphology (Figure 1d and e), indicating the reconstruction of Fe_3O_4 nanoparticles during the carbonization of glucose (600 °C for 4 h). During heat treatment, the smaller primary nanoparticles of Fe_3O_4 will merge into bigger ones due to the grain-boundary migration with the lattice diffusion of oxygen.[19] Notably, it is much brighter in the core of the Fe_3O_4@C for TEM images (Supporting information S2), demonstrating that all of the spheres have a hollow interior. Comparing with template-assisted methods for hollow structures, which requires a complicated procedure of preparation/removal of templates and suffers from partial structural collapse during the removal of templates,[11a] this procedure is quite simple and effective. It is believed that such a unique geometrically hierarchical structure confined by carbon can effectively suppress the aggregation of nanoparticles and enhance electrode stability against cycling processes for lithium storage.

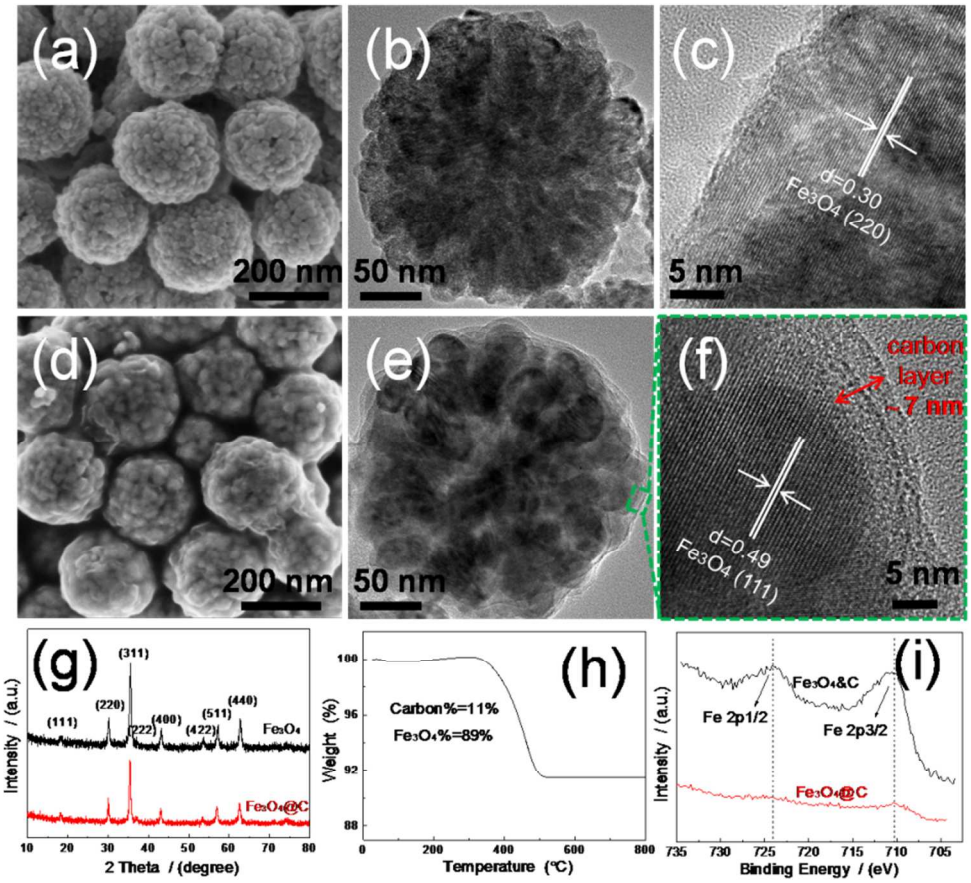

Fig.1 a), b) and c) are the SEM, TEM and HRTEM images of hierarchical Fe_3O_4 spheres; d), e) and f) are the SEM, TEM and HRTEM images of hierarchical Fe_3O_4@C core-shell spheres; g) XRD patterns of Fe_3O_4 and Fe_3O_4@C spheres; h) TGA profile of Fe_3O_4@C spheres; i) High-resolution XPS Fe 2p spectrum of mixture of Fe_3O_4&C (89:11 in mass) and Fe_3O_4@C spheres;

Phase structure and composition of the sample were further identified by XRD, TGA and XPS. XRD patterns of the as-synthesized Fe_3O_4 and Fe_3O_4@C hollow spheres are shown in Figure 1g. It is found that all the diffraction peaks can be well indexed to the magnetic cubic structure of Fe_3O_4 (JCPDS 79-0419). After coating carbon, no other peaks show up, indicating the carbon is in amorphous state, in good agreement with the HRTEM results. To determine the chemical composition of hybrid Fe_3O_4@C composite, TGA was performed as shown in Figure 1h. The sample was heated to 800 °C in air so that Fe_3O_4 is oxidized to Fe_2O_3 and carbon is oxidized to CO_2. According to the remaining weight of Fe_2O_3, the original fraction of Fe_3O_4 is calculated to be 89 wt%, which is much higher than those reported for Fe_3O_4/carbon composites.[16c, 20] In order to further confirm if our synthesized Fe_3O_4@C core-shell spheres have a high-quality encapsulation structure, a surface-sensitive high-resolution XPS experiment was carried out to examine the chemical characteristics of the surface of the spheres. For comparison, a mixture of Fe_3O_4 and graphite (Fe_3O_4&C) with weight ratio of 89:11 was also tested. Figure S3 shows the full XPS spectrums of the Fe_3O_4@C and Fe_3O_4&C, in which the photoelectron lines at a binding energy of about 285 and 532 eV are attributed to C 1s and O 1s, respectively. Figure 1(i) exhibits the high-resolution XPS Fe 2p spectrum of Fe_3O_4&C (89:11 in mass) and Fe_3O_4@C spheres. Intensive peaks of Fe $2p_{3/2}$ and Fe $2p_{1/2}$ at about 710 and 724 eV for the mixture of Fe_3O_4&C can be observed, but there is almost an absence of the signals of Fe $2p_{3/2}$ and Fe $2p_{1/2}$ for the Fe_3O_4@C composite. Because the atomic sensitivity factor of Fe is much higher than those of C and O,[14] absence of its peaks implies that, in our synthesized Fe_3O_4@C core-shell spheres, the Fe_3O_4 spheres appears to be completely sealed inside the carbon shells. It is believed that the entire core-shell structure will be more favorable to keep the architecture integrity during electrochemical discharge and charge processes comparing with the bare spheres or the carbon supported spheres.[16a, 21]

The porous structure of hybrid Fe_3O_4@C was further probed by nitrogen isothermal adsorption/desorption measurement (Figure 2). Remarkably, the Brunauer-Emmett-Teller specific surface area of Fe_3O_4@C was calculated to be 52.0 m^2/g which is higher than that of Fe_3O_4 spheres (34.9 m^2/g). We obtained a type-IV isotherm for the Fe_3O_4 spheres with an H3-type hysteresis loop attributed to a mesoporous system as is frequently observed for porous materials with broad pore-size distributions.[5, 22] The pore size distribution for the Fe_3O_4 spheres is shown in the inset of Figure 2a and indicates the formation of randomly distributed pores with size of from 4 to 15 nm and dominant at 4 nm. Interestingly, a well-defined 4 nm mesopore distribution with much higher intensity was obtained for Fe_3O_4@C from analysis of the isotherms (inset of Figure 2b), which can be attributed to the intervoids among the constituent nanoparticles. Uniform pores of Fe_3O_4@C imply the reconstruction of nanoparticles of Fe_3O_4 during carbon coating, which is in consistent with the SEM and TEM observations. For the big pores with large open-windows, the glucose may access to the pores and form the conducting carbon networks for the Fe_3O_4@C, which can improve the rate performance of the Fe_3O_4@C electrode. The high specific surface area of hybrid Fe_3O_4@C in association with its uniform mesoporous features, are favorable for electrolyte accessibility and rapid lithium-ion diffusion.[16c] Based on the BET data, the specific pore volumes of Fe_3O_4 and Fe_3O_4@C are calculated to be 0.1006 cm^3/g and 0.0660 cm^3/g, respectively. High volumetric capacities of 3150 mAh/cm^3 and 2950 mAh/cm^3 are achieved for Fe_3O_4 and Fe_3O_4@C, respectively.

The electrochemical performance was evaluated by preparing coin-type half cells that employ Fe_3O_4@C as a working electrode and Li foil as a counter/reference electrode. In this study the capacity is calculated based on the total mass of the composite including Fe_3O_4 and carbon shells. In order to clearly demonstrate superior features of Fe_3O_4@C on electrochemical performance, Fe_3O_4 spheres were also examined. Figure 3a and b represent the cyclic voltammograms of the Fe_3O_4@C and Fe_3O_4, respectively. In the cathodic process, both samples showed large peak at ~ 0.5 V in the first cycle, indicating the reaction $Fe_3O_4 + 8Li^+ + 8e^- \rightarrow 3Fe^0 + 4Li_2O$ with the formation of the SEI layer. In

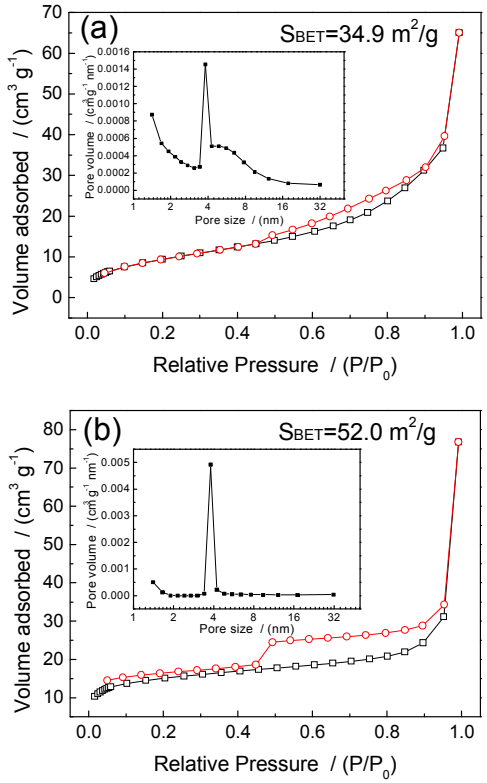

Fig.2 N_2 adsorption-desorption isotherms of Fe_3O_4 (a) and hybrid Fe_3O_4@C (b), and corresponding pore-size distributions of Fe_3O_4 (inset of a) and Fe_3O_4@C (inset of b).

the first anodic process, two peaks were observed at 1.68 and 1.85 V in Fe_3O_4@C, attributed to the oxidation of Fe^0 to Fe^{2+} and Fe^{3+}, respectively.[5, 14] The difference between the peaks in the first cycle and subsequent cycles can be ascribed to activation processes, including the conversion to nanosized metal particles

dispersed in the Li_2O matrix or the formation of the SEI layers.[5] For the bare Fe_3O_4 electrode, much broad peaks were observed in the anodic processes, while the intensity lowered compared with the first cycle, indicating that an irreversible transformation occurred.

Figure 3c and d show the charge/discharge curves of the Fe_3O_4@C and Fe_3O_4 electrodes at rate of 1 A/g in the voltage range of 0.05-3 V (versus Li^+/Li). Upon cycling, the first discharge and charge capacities of the Fe_3O_4@C electrode were as high as 1226 and 862 mAh g^{-1}, delivering an initial Coulombic efficiency of ~70%. In contrast, the bare Fe_3O_4 spheres deliver a relatively low Coulombic efficiency of 58%. The irreversible capacity loss of the first cycle could be ascribed to the inevitable formation of a surface SEI layer accompanying the electrolyte decomposition during discharge.[23] Quite interestingly, the cycling performance of Fe_3O_4@C seems undergo three stages upon repeated cycling. The discharge voltage plateau at ~0.7 V in the first cycle is different from those of other cycles (2nd, 3rd and 100th) at ~1.0 V, further implying that irreversible reactions occurred in the first cycle. In the subsequent cycling, no obvious change in both charge and discharge profiles is observed for the 2nd, 3rd and even the 100th cycle, which indicates that the carbon shells safeguard the structural integrity of Fe_3O_4 active materials during subsequent cycles, leading to the stable and superior reversibility of the electrodes. As cycling number increases (200th, 400th, 600th), the discharge/charge voltage plateau was less obvious with a capacity higher than the theoretical specific capacity of the composite (Fe_3O_4, 926 mAh g^{-1} and graphite, 372 mAh g^{-1}). The excess capacity and the increasing trend in the repeated cycles is likely due to the reversible growth of the polymeric gel-like film by the kinetically activated electrolyte degradation, which has been also observed in other metal oxide composites[16c, 16d, 24], or further lithium storage as a result of interface reaction in the process of activation and stabilization of the electrode.[23] In the case of bare Fe_3O_4 spheres, the SEI films will rupture due to the mechanical strain generated by the volume expansion/contraction during cycling or the catalyzing by the Fe nanocrystals formed during the delithiation processes, and thus the electrode surface would be cyclically exposed to the electrolyte, which results in continual formation of thick SEI films and accordingly continual consuming of electrolyte.[14] The cyclical rupture and growth of SEI will cause low Coulombic efficiency, higher resistance to ionic transport, and low electronic conductivity of the whole electrode.[15, 25] Therefore, the capacity of the anode of bare Fe_3O_4 spheres decreases rapidly, and their cycling performance is remarkably worse than that of Fe_3O_4@C core-shell spheres.

Figure 3e shows cycling performance of Fe_3O_4, Fe_3O_4@C and the corresponding Coulombic efficiency of the Fe_3O_4@C electrode under a current density of 1 A g^{-1}. Interestingly, the capacity of the Fe_3O_4@C initially decreased until the 6 cycles and then started to increase until 200th cycle. A high reversible capacity of 910 mAh g^{-1} was obtained even after 600th cycles, which is higher than that of Sn-Co-C anode proposed by Sony company.[3] Such high capacity retention of iron oxide electrode at a current rate of 1 A g^{-1} after hundreds cycling is few reported. As compared to other iron oxide anodes tested under similar conditions, our hierarchical Fe_3O_4@C core-shell structure reveals greatly enhanced lithium storage properties with a higher reversible capacity.[7b, 10] The superior performance could probably be attributed to the nanometer-sized subunits with surrounding mesopores and the conducting carbon shells, which have been verified by SEM, TEM and BET techniques. After repeated electrochemical cycling, the primary Fe_3O_4 nanoparticles pulverized into the smaller ones, the internal mesopores allow the iron oxide to effectively buffer the volume change during discharge-charge processes, while the outside carbon layers can ensure the structural integrity. The carbon shells associated with the internal pores provide a fast and efficient transport of electron and Li ions. In contrast, Fe_3O_4 spheres showed a capacity of 850 mAh g^{-1} initially but faded gradually. After 200th cycle, they exhibited about 48 % of capacity retention, and the measurement was ceased. Although the hierarchical Fe_3O_4 spheres can alleviate the crumbling of Fe_3O_4 to some extent because of the inter-voids,[26] and exhibit an improved electrochemical performance compared with solid counterpart, the excessive generation of SEI on the surface associated with the disintegration aroused by crack-up result in a degradation of electrochemical performance. The rate performance of the hierarchical Fe_3O_4@C electrode is also outstanding (Figure S4). It can deliver high average specific capacities of 900, 850, 610, 380 and 200 mAh g^{-1} at the current densities of 0.5, 1, 4, 10 and 20 C (1 C = 926 mA/g), respectively. More interestingly, when the current rate was reduced stepwise to 0.5 C after 160 cycles, the stable high capacity of 900 mAh g^{-1} for Fe_3O_4@C was resumed. Although the intrinsically high plateau of Fe_3O_4 will suppress the energy density compared with graphite when it is used as anode material, while the significantly increased capacity will play a more important role in enhancing the energy density. Besides, the Fe_3O_4 with relatively higher operating voltage can avoid the safety issues especially in the higher discharge-charge rate.[4a]

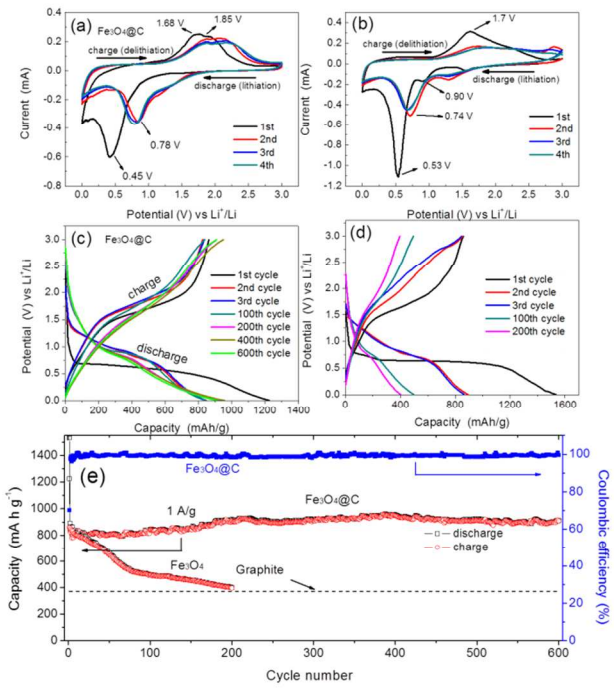

Fig. 3 Electrochemical performance of Fe_3O_4@C spheres and Fe_3O_4

spheres: (a) and (b) representative CV curves of hierarchical Fe_3O_4@C spheres and Fe_3O_4 obtained at a range of 0.0 to 3.0 V (vs. Li^+/Li) and potential scan rate of 0.1 mV/s; (c) and (d) charge/discharge curves of Fe_3O_4@C and Fe_3O_4 electrode; (e) Cycling performance for Fe_3O_4@C and Fe_3O_4 electrode at a current density of 1 A/g.

To verify the superior electrochemical performance of hierarchical Fe_3O_4@C spheres, electrochemical impedance measurements were performed after five discharge-charge cycles. The Nyquist plots for the samples are shown in Figure 4 with a frequency range of 100 kHz to 0.01 Hz. The diameter of the semicircle for hybrid hierarchical Fe_3O_4@C electrode in the high-medium frequency region is much smaller than that of Fe_3O_4. The value of R_{ct} is ~36 Ω for the hierarchical Fe_3O_4@C composite, which is lower than that of corresponding Fe_3O_4 spheres (78 Ω). It can be attributed to the increased contact area at the electrode/electrolyte interface as well as the enhanced electrical conductivity of the overall electrode.[16b, 27] At the low frequency region, a more vertical straight line of the Fe_3O_4@C compared to the Fe_3O_4 is further evident for the faster Li^+ ion diffusion behavior of the hierarchical Fe_3O_4@C electrode. Once again, it is further evidenced the unique structure of hierarchical Fe_3O_4@C hollow spheres on the contribution to the enhanced cycling and rate capability compared to the bare Fe_3O_4 hollow spheres

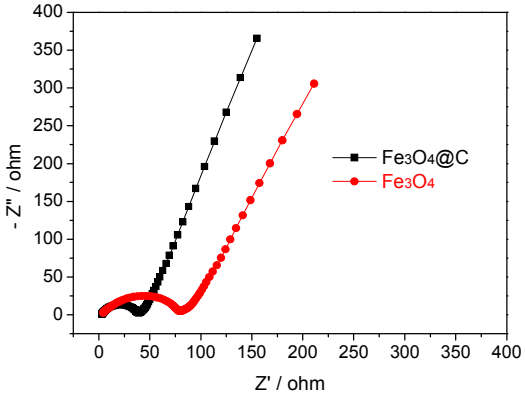

Fig.4 Nyquist plots (100 kHz – 10 mHz) of Fe_3O_4 and hierarchical Fe_3O_4@C electrodes.

The different morphology and structure features during cycling between the Fe_3O_4 spheres and hybrid Fe_3O_4@C spheres play an important role in cycling stability, which are validated by SEM and TEM investigations after discharge/charge cycles. The original morphology of the hybrid Fe_3O_4@C electrode is well preserved by coating the porous hollow Fe_3O_4 spheres with a carbon shell, as shown in Figure 5a, b and c. In contrast to the speckles and distinct rings for the initial Fe_3O_4@C materials (Figure S2), diffusion rings are observed in the SAED pattern (inset, Figure 5c), indicating the encapsulated nanoparticles of Fe_3O_4 were pulverized. The HRTEM image (Figure 5d and e) evidences that Fe_3O_4 nanoparticles have been pulverized but are still sealed in the carbon layers. In contrast, the bare Fe_3O_4 electrode was totally breakdown and could not find any spheres after 50 cycles at a cycling rate of 1 A g^{-1} (Figure S5). XRD patterns for Fe_3O_4@C electrode are shown in Figure 5f. The significantly broad bumps with low intensity for Fe_3O_4 after cycling confirm the dramatic reduction of grain size. Apart from Fe_3O_4, no other phases show up, indicating the excellent reversibility of electrochemical processes. We also conducted the SEM/TEM characterizations for the cycled Fe_3O_4@C material in the charged state. In the TEM experiment, SAED patterns were carried out. All of the images (Figure S6 and S7) are supplemented in the supporting information. Most of the Fe_3O_4@C composites were kept in the spherical shape, among which the carbon black and binder can be clearly observed. After several cycles, the lithiated Fe_3O_4@C composite is in relatively low crystallinity, thus only several diffuse rings can be observed in the SAED patterns, which can be ascribed to the *in situ* formed Fe nanocrystals. Based on the above analysis, a scheme of the microstructure evolvement of hierarchical Fe_3O_4@C hollow electrode is illustrated in Figure 5g. During repeated charge/discharge, the constituent nanoparticles of Fe_3O_4 pulverized into smaller ones, the stress of which can be sufficiently accommodated by the inter-voids, while the carbon shells can prevent the exfoliation and disconnection of active materials and effectively cage these pulverized particles. Therefore, the overall structural stability and durability of the electrode are improved.

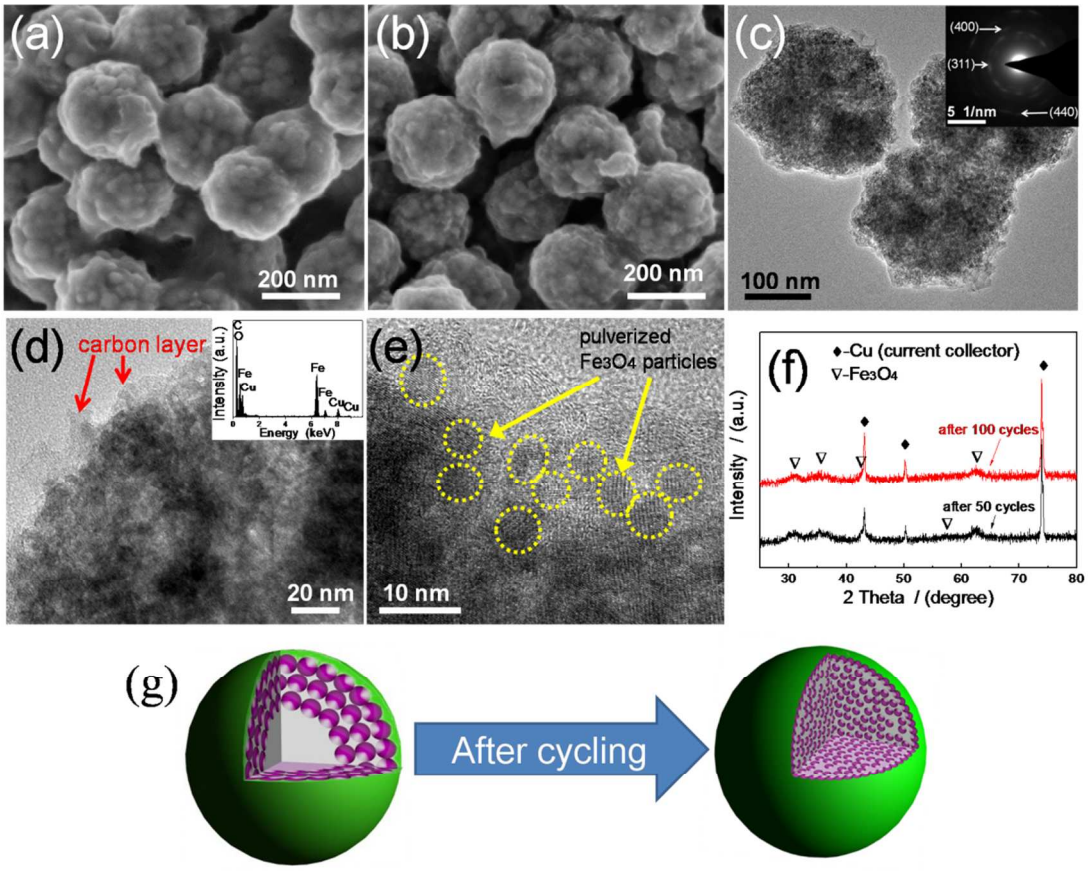

Fig. 5. SEM images of Fe_3O_4@C electrode after 10 (a) and 50 (b) cycles. TEM images of Fe_3O_4@C electrode after 100 cycles (c), (d) and (e). The insets of (c) and (d) are the corresponding SAED patterns and EDS results. The presence of Cu is derived from the copper mesh that supports the sample during TEM measurement. (f) XRD patterns of Fe_3O_4@C electrode after different cycles. The presence of Cu is derived from current collector. (g) A schematic illustration of cycling effects on the microstructure evolvement of Fe_3O_4@C electrode.

To evaluate the performance of Fe_3O_4@C material, a full-cell battery with the commercial cathode of $LiMn_2O_4$ and the as-prepared Fe_3O_4@C as anode was fabricated. The cycling performance is shown in Figure S8. As expected, a discharge plateau of ~ 2.5 V and charge plateau of ~ 3.3 V can be observed during cycling test. After 50th cycling at a 1C rate, the capacity of Fe_3O_4@C can still exhibit a capacity of ~ 800 mAh g^{-1}. The favourable cycling stability of Fe_3O_4@C in the full-cell battery makes it a promising anode material for LIBs.

4. Conclusions

In summary, 3D hierarchical Fe_3O_4@C electrode comprising mesoporous Fe_3O_4 spheres with carbon shells was fabricated. The unique architecture for the hybrid electrode endows a structural and electrochemical integrity for the composite during repeated electrochemical cycling, and ensures favorable transport kinetics for both electrons and lithium ions. As a consequence, superior cycling performance (910 mAh g^{-1} at 1 A g^{-1} over 600 cycles) and excellent rate capability (380 mAh g^{-1} at 10 C) were achieved. The outstanding electrochemical performance of the hybrid electrode can be ascribed to the following reasons: 1) the outer shell of carbon can form a stable SEI layer on the surface and inhibit the aggregation of pulverized Fe_3O_4 in electrochemical cycling; 2) the hierarchical structure can efficiently accommodate the mechanical stress induced by the volume variation of Fe_3O_4 during lithiation/delithiation processes; 3) the carbon layers in association with mesoporous structural provide a fast and efficient transport of electron and Li ions. Such a simple and scalable route to construct carbon encapsulated hierarchical core-shell structure may be further extended to other metals or metal oxides for electrochemical energy storage applications.

Acknowledgements

The authors gratefully acknowledge the support of the National Natural Science Foundation of China (21303161, 51171173 and 51001090), the Key Science and Technology Innovation Team of Zhejiang Province (2010R50013), the China Postdoctoral Science Foundation (2012M521167) and the Chinese Postdoctoral International Exchange Program (2013).

Notes and References

State Key Laboratory of Silicon Materials, Key Laboratory of Advanced Materials and Application for Batteries of Zhejiang Province, Department of Materials Science and Engineering, Zhejiang University, Hangzhou 310027, PR China. E-mail:lxchen@zju.edu.cn

† Electronic Supplementary Information (ESI) available: [SEM images of Fe_3O_4 and Fe_3O_4@C spheres, TEM image for the hybrid Fe_3O_4@C spheres and corresponding SAED patterns, XPS survey scans of mixture of Fe_3O_4 nanospheres with graphite (weight, 89:11) and as-prepared hybrid Fe_3O_4@C composite, Charge/discharge rate properties of hybrid

Fe_3O_4@C electrode, SEM image for bare Fe_3O_4 sphere electrode after 50th cycles, SEM image of the Fe_3O_4@C electrode in the charged state, TEM image and the corresponding SAED pattern of the Fe_3O_4@C electrode in the charged state, charge-discharge curves for the full-cell battery with the commercial cathode of $LiMn_2O_4$ and the as-prepared Fe_3O_4@C as anode]. See DOI:10.1039/b000000x/

[1] (a) F.Y. Cheng, J. Liang, Z.L. Tao, J. Chen, *Adv. Mater.*, 2011, **23**, 1695-1715; (b) Y. Wu, Y. Wei, J. Wang, K. Jiang, S. Fan, *Nano Lett.*, 2013, **13**, 818-823; (c) Y.X. Yin, S. Xin, Y.G. Guo, *Part. Part. Sys. Charact.*, 2013, **30**, 737-753; (d) N. Nitta, G. Yushin, *Part. Part. Sys. Charact.*, 2014, **31**, 317-336.

[2] (a) J. Luo, X. Xia, Y. Luo, C. Guan, J. Liu, X. Qi, C.F. Ng, T. Yu, H. Zhang, H. J. Fan, *Adv. Energy Mater.*, 2013, **3**, 737-743; (b) D. Chen, G. Ji, Y. Ma, J. Y. Lee, J. Lu, *Acs Appl. Mater. Inter.*, 2011, **3**, 3078-3083.

[3] (a) V. Aravindan, J. Gnanaraj, Y.S. Lee, S. Madhavi, *J. Mater. Chem. A*, 2013, **1**, 3518-3539; (b) M.M. Thackeray, C. Wolverton, E.D. Isaacs, *Energy Environ. Sci.*, 2012, **5**, 7854-7863.

[4] (a) L. Zhang, H.B. Wu, X.W. Lou, *Adv. Energy Mater.*, 2013, DOI: 10.1002/aenm.201300958; (b) J. Cabana, L. Monconduit, D. Larcher, M.R. Palacín, *Adv. Mater.*, 2010, **22**, E170-E192; (c) Y.L. Wang, L. Zhang, X.H. Gao, L.Y. Mao, Y. Hu, X.W. Lou, *Small*, 2014, DOI: 10.1002/smll.201400239.

[5] S.H. Lee, S.H. Yu, J.E. Lee, A. Jin, D.J. Lee, N. Lee, H. Jo, K. Shin, T.Y. Ahn, Y.W. Kim, H. Choe, Y.E. Sung, T. Hyeon, *Nano Lett.*, 2013, **13**, 4249-4256.

[6] (a) M.V. Reddy, G.V. Subba Rao, B.V.R. Chowdari, *Chem. Rev.*, 2013, **113**, 5364-5457; (b) Z.S. Wu, G.M. Zhou, L.C. Yin, W. Ren, F. Li, H.M. Cheng, *Nano Energy*, 2012, **1**, 107-131; (c) R. Mukherjee, R. Krishnan, T.M. Lu, N. Koratkar, *Nano Energy*, 2012, **1**, 518-533; (d) A. Banerjee, V. Aravindan, S. Bhatnagar, D. Mhamane, S. Madhavi, S. Ogale, *Nano Energy*, 2013, **2**, 890-896.

[7] H.S. Lim, Y.K. Sun, K.D. Suh, *J. Mater. Chem. A*, 2013, **1**, 10107-10111; (b) M. Biswal, A. Suryawanshi, V. Thakare, S. Jouen, B. Hannoyer, V. Aravindan, S. Madhavi, S. Ogale, *J. Mater. Chem. A*, 2013, **1**, 13932-13940.

[8] (a) J. Zhu, Z. Yin, D. Yang, T. Sun, H. Yu, H.E. Hoster, H.H. Hng, H. Zhang, Q. Yan, *Energy Environ. Sci.*, 2013, **6**, 987-993; (b) Y. Xu, G. Jian, Y. Liu, Y. Zhu, M.R. Zachariah, C. Wang, *Nano Energy*, 2014, **3**, 26-35; (c) J.S. Xu, Y.J. Zhu, *Acs Appl. Mater. Inter.*, 2012, **4**, 4752-4757;

[9] (a) J. Miot, N. Recham, D. Larcher, F. Guyot, J. Brest, J.M. Tarascon, *Energy Environ. Sci.*, 2014, **7**, 451-460; (b) R. Wang, C. Xu, J. Sun, L. Gao, C. Lin, *J. Mater. Chem. A*, 2013, **1**, 1794-1800.

[10] (a) G. Gao, Q. Zhang, K. Wang, H. Song, P. Qiu, D. Cui, *Nano Energy*, 2013, **2**, 1010-1018; (b) L.H. Zhuo, Y.Q. Wu, L.Y. Wang, J. Ming, Y.C. Yu, X.B. Zhang, F.Y. Zhao, *J. Mater. Chem. A*, 2013, **1**, 3954-3960.

[11] (a) J. Liu, Y. Li, H. Fan, Z. Zhu, J. Jiang, R. Ding, Y. Hu, X. Huang, *Chem. Mater.*, 2009, **22**, 212-217; (b) Z. Wang, D. Luan, S. Madhavi, C. Ming Li, X.W. Lou, *Chem. Commun.*, 2011, **47**, 8061-8063; (c) N. Kang, J.H. Park, J. Choi, J. Jin, J. Chun, I.G. Jung, J. Jeong, J.G. Park, S.M. Lee, H.J. Kim, S.U. Son, *Angew. Chem. Int. Ed.*, 2012, **51**, 6626-6630.

[12] (a) S. Xu, C. M. Hessel, H. Ren, R. Yu, Q. Jin, M. Yang, H. Zhao, D. Wang, *Energy Environ. Sci.*, 2014 DOI:10.1039/C3EE43319F; (b) H.S. Lim, Y.K. Sun, K.D. Suh, *J. Mater. Chem. A*, 2013, **1**, 10107-10111; (c) R.H. Wang, C.H. Xu, J. Sun, L. Gao, C.C. Lin, *J. Mater. Chem. A*, 2013, **1**, 1794-1800.

[13] (a) B. Koo, H. Xiong, M.D. Slater, V.B. Prakapenka, M. Balasubramanian, P. Podsiadlo, C.S. Johnson, T. Rajh, E.V. Shevchenko, *Nano Lett.*, 2012, **12**, 2429-2435; (b) J.S. Chen, T. Zhu, X.H. Yang, H.G. Yang, X.W. Lou, *J. Am. Chem. Soc.*, 2010, **132**, 13162-13164.

[14] C. He, S. Wu, N. Zhao, C. Shi, E. Liu, J. Li, *ACS Nano*, 2013, **7**, 4459-4469.

[15] Y.G. Guo, J.S. Hu, L.J. Wan, *Adv. Mater.*, 2008, **20**, 2878-2887.

[16] (a) J.S. Chen, Y. Zhang, X.W. Lou, *Acs Appl. Mater. Inter.,* 2011, **3**, 3276-3279; (b) J.M. Jeong, B.G. Choi, S.C. Lee, K.G. Lee, S.J. Chang, Y.K. Han, Y.B. Lee, H.U. Lee, S. Kwon, G. Lee, C.S. Lee, Y.S. Huh, *Adv. Mater.*, 2013, **25**, 6250-6255; (c) W. Wei, S. Yang, H. Zhou, I. Lieberwirth, X. Feng, K. Müllen, *Adv. Mater.*, 2013, **25**, 2909-2914; (d) G. Zhou, D.W. Wang, F. Li, L. Zhang, N. Li, Z.S. Wu, L. Wen, G.Q. Lu, H.M. Cheng, *Chem. Mater.*, 2010, **22**, 5306-5313; (e) Y. Chang, J. Li, B. Wang, H. Luo, H. He, Q. Song, L. Zhi, *J. Mater. Chem. A*, 2013, **1**, 14658-14665; (f) S.Q. Chen, P. Bao, G.X. Wan, *Nano Energy*, 2013, **2**, 425-434; (g) X. Wang, W. Tian, D. Liu, C. Zhi, Y. Bando, D. Golberg, *Nano Energy*, 2013, **2**, 257-267; (h) J. Luo, J. Liu, Z. Zeng, C. F. Ng, L. Ma, H. Zhang, J. Lin, Z. Shen, H.J. Fan, *Nano Lett.*, 2013, **13**, 6136-6143; (i) Y. Chen, B.H. Song, X.S. Tang, L. Lu, J.M. Xue, *J. Mater. Chem.*, 2012, **22**, 17656-17662.

[17] (a) W.M. Zhang, X.L. Wu, J.S. Hu, Y.G. Guo, L.J. Wan, *Adv. Funct. Mater.*, 2008, **18**, 3941-3946; (b) T. Zhu, J.S. Chen, X.W. Lou, *J. Phys. Chem. C*, 2011, **115**, 9814-9820; (c) W. Shi, X. Rui, J. Zhu, Q. Yan, *J. Phys. Chem. C*, 2012, **116**, 26685-26693.

[18] E. Kang, Y.S. Jung, A.S. Cavanagh, G.H. Kim, S.M. George, A.C. Dillon, J.K. Kim, J. Lee, *Adv. Funct. Mater.*, 2011, **21**, 2430-2438.

[19] M.F. Yan, *J. Am. Ceram. Soc.*, 1980, **63**, 443-447.

[20] W.J. Yu, P.X. Hou, F. Li, C. Liu, *J. Mater. Chem.*, 2012, **22**, 13756-13763.

[21] T.Q. Wang, X.L. Wang, Y. Lu, Q.Q. Xiong, X.Y. Zhao, J.B. Cai, S. Huang, C.D. Gu, J.P. Tu, *RSC Adv.*, 2014, **4**, 322-330.

[22] J.L. Mohanan, I.U. Arachchige, S.L. Brock, *Science*, 2005, **307**, 397-400.

[23] X. Xu, R. Cao, S. Jeong, J. Cho, *Nano Lett.*, 2012, **12**, 4988-4991.

[24] (a) J.S. Do, C.H. Weng, *J. Power Sources*, 2005, **146**, 482-486; (b) Y. Xu, J. Guo, C. Wang, *J. Mater. Chem.*, 2012, **22**, 9562-9567.

[25] A.S. Arico, P. Bruce, B. Scrosati, J.M. Tarascon, W. van Schalkwijk, *Nature Mater.*, 2005, **4**, 366-377.

[26] Q.Q. Xiong, J.P. Tu, Y. Lu, J. Chen, Y.X. Yu, Y.Q. Qiao, X.L. Wang, C.D. Gu, *J. Phys. Chem. C*, 2012, **116**, 6495-6502.

[27] B.G. Choi, M. Yang, W.H. Hong, J.W. Choi, Y.S. Huh, *ACS Nano*, 2012, **6**, 4020-4028.